Ideal Shear Strength of a Quantum Crystal

Edgar Josué Landinez Borda,[1,†] Wei Cai,[2,‡] and Maurice de Koning[1,*]
[1]Instituto de Física "Gleb Wataghin," Universidade Estadual de Campinas, UNICAMP, 13083-859 Campinas, São Paulo, Brazil
[2]Department of Mechanical Engineering, Stanford University, Stanford, California 94305-4040, USA
(Received 30 December 2013; published 17 April 2014)

Using path-integral Monte Carlo simulations, we compute the ideal shear strength (ISS) on the basal plane of hcp ^{4}He. The failure mode upon reaching the ISS limit is characterized by the homogeneous nucleation of a stacking fault and it is found to be anisotropic, consistent with Schmid's law of resolved shear stress. Comparing the ISS of hcp ^{4}He to a large set of classical crystals shows that it closely fits the approximately universal modified Frenkel model of ideal strength. In addition to giving quantitative stress levels for the homogeneous nucleation of extended defects in hcp ^{4}He, our findings lend support to assumptions in the literature that inherently classical models remain useful for the description of mechanical behavior in quantum crystals.

DOI: 10.1103/PhysRevLett.112.155303 PACS numbers: 67.80.B-, 61.72.Nn, 62.20.F-

The ideal strength (IS) of a solid is defined as the maximum stress that, for a given loading mode, an infinite defect-free specimen can withstand [1–3]. It represents a theoretical upper limit to the resistance to deformation before yielding irreversibly. An important example is the ideal shear strength (ISS), which is defined as the maximum shear stress a perfect crystal can resist [3]. In addition to the fact that in some systems such theoretical limits can actually be closely approached [4–10], they represent fundamental material parameters that are closely involved in the nucleation of defects and in the theory of fracture [11–13].

The IS concepts have, so far, been investigated only in the context of classical crystals in which the quantum-mechanical effects are mostly negligible [2,3,14–18]. Recently, however, there has been a growing interest in the deformation behavior of so-called quantum crystals, in which such quantum fluctuations are dominant [19]. A particularly important case concerns that of the archetypal bosonic quantum solid, crystalline ^{4}He [20–30]. Despite the increasing sophistication of recent experiments, their interpretation must often rely on assumptions. This has led to controversy and conflicting views [31,32], in part due to the lack of knowledge of fundamental material parameters such as the IS, which are inaccessible experimentally.

In this Letter, we determine the IS for the hcp ^{4}He quantum crystal. In particular, we focus on the ISS associated with affine shear deformations in the basal plane, on which plasticity is known to predominantly occur [29,33]. For this purpose, we rely on fully correlated quantum simulations based on the path-integral Monte Carlo (PIMC) method which has been widely applied for the condensed phases of ^{4}He [34–42]. Not only do our results establish quantitative stress levels for the nucleation of extended defects in hcp ^{4}He, they also extend to the realm of quantum solids the modified Frenkel model [3,43], which has been shown to provide an approximately universal scaling relation for the ISS of many classical crystals characterized by different crystal structures, bonding types, and slip systems [3]. Furthermore, this surprising finding seems to lend support to the assumptions mentioned in the previous paragraph.

We determine the ISS in the basal plane of hcp ^{4}He at a fixed molar volume of 21 cm^3. We employ fully periodic cells containing $N = 180$ (small), $N = 480$ (medium), and $N = 720$ (large) atoms, respectively, all characterized by the ideal ratio $c/a = 1.633$. Having the same size along the c axis, the size difference between these cells is due to different basal-plane areas. To assess the influence of thermal versus quantum fluctuations, ISS calculations are carried out for a series of temperatures between 2 and $2/15$ K. All simulations have been carried out using the PIMC++ package [36], which is a C++ implementation of the PIMC algorithms described in Ref. [34]. The used pair action was obtained from a standard matrix squaring procedure [34,44] using the Aziz HFD-B3-FCI1 pair potential [45] imposing an interaction cutoff of 8 Å. This cutoff is larger than that used by Ceperley and Pollock [46] in their study of liquid ^{4}He and in which excellent agreement with experiment was observed. To estimate the role of path-discretization errors, we employ time steps between $\tau \equiv \beta/M = 1/40$ K^{-1} and $\tau = 1/320$ K^{-1} [47], with β the inverse temperature and M the number of beads in the ring polymers. Sampling was parallelized over beads, with each processor handling five beads of all particles at any instant, and a MC step is defined as a sequence of N fixed-box two-level permutation and bisection trial moves [34] per processor. The calculation of the stress observable was carried out as described in Ref. [42]

For each condition of temperature, cell size, and time step, the ISS is determined by creating a sequence of states

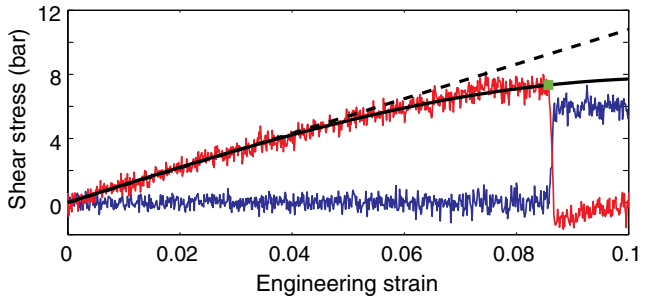

FIG. 1 (color online). Typical shear stress response as a function of strain. Upper (red) and lower (blue) irregular lines denote stress components parallel and perpendicular to direction of applied strain, respectively. Dashed black line represents linear elastic response as determined in Ref. [42]. Solid smooth (black) line represents sinusoidal fit to data. Corresponding ideal strain and stress values are denoted by the square.

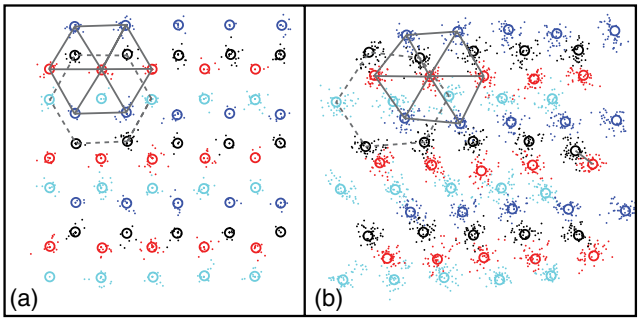

FIG. 2 (color online). Snapshots of centroid (circles) and bead (dots) positions of two adjacent atomic basal planes at different stages of deformation. (a) Zero deformation. (b) Immediately after discontinuity in shear stress.

of increasing homogeneous volume-conserving shear deformation. This is achieved by incrementing the in-plane component of the periodic box repeat vector initially pointing along the c axis in a specified direction in the basal plane at a given deformation rate $\dot{d}$, which is defined as the magnitude of the in-plane displacement (in Å) per MC step. We use four different deformation rates: $\dot{d} = 5 \times 10^{-6}$, 2×10^{-6}, 1×10^{-6}, and 5×10^{-7} Å per MC step. The ISS is then determined by monitoring the in-plane stress component associated with the applied shear. A typical example of the in-plane shear stress response to the increasing deformation is shown in Fig. 1, obtained with $N = 720$, $T = 1$ K, $\tau = 1/40$ K^{-1}, and $\dot{d} = 5 \times 10^{-6}$ Å per step. As expected, the shear-stress response for the component parallel to the deformation is initially linear elastic with slope equal to the shear modulus computed in Ref. [42], followed by a nonlinear elastic regime. The sudden jump at a critical strain value of 8.4%, which we will refer to as shearability, indicates that the ISS limit has been reached. The associated stress value is then determined from the stress-strain curve, which is obtained by fitting a sinusoidal to the data, as shown by the solid black line. The resulting data point for the pair of shearability and critical stress from this particular simulation is depicted by the square. Because of the thermal and quantum fluctuations, the ISS measurement is subject to statistical uncertainty and to gather statistics we carry out between 5 and 15 independent simulations for each deformation process. Given that the result of each simulation is an upper limit to the true values due to the finite deformation rate (see Supplemental Material [48]), we define our estimate for the shearability and the ISS as the lowest critical strain value in the set and its associated critical stress value obtained from the stress-strain curve, respectively.

First, we examined the failure mode by which the elastic behavior is interrupted as the ISS limit is reached. To this end, we monitor the atomic planes normal to the c axis during the straining process. Figure 2 shows two snapshots of adjacent atomic basal planes at different stages of deformation for the same simulation conditions as those of Fig. 1. The open circles represent the centroids of the paths and the small colored dots show individual bead positions. Figure 2(a) depicts an instant in which no shear deformation is applied. The packing structure shows the usual $\cdots ABAB \cdots$ pattern characteristic of the hcp structure. Figure 2(b), on the other hand, shows the same two planes immediately after the discontinuity of the type shown in Fig. 1. It is clear that the jump in the shear stress has been caused by one plane slipping over the other, producing a stacking fault (SF). In all our simulations, the attainment of ISS value is accompanied by such a nucleation event, regardless of system size, temperature, time step, deformation direction, and deformation rate. Interestingly, this mechanism is precisely the same as that seen in typical classical crystals with a close-packed crystal structure [16].

Next, we investigate the anisotropy of the basal-plane ISS. To this end, we analyze results obtained for the cell with $N = 180$ atoms, $T = 1$ K, $\tau = 1/40$ K^{-1}, and a deformation rate $\dot{d} = 1 \times 10^{-6}$ for 12 different directions in the basal plane, described in terms of the angle θ with respect to the positive x axis of Fig. 3(a). We consider values between $\theta = 0°$ and 330° in steps of 30° and carry out five independent simulations for each direction. The results are shown in the polar plot in Fig. 3(b), which displays the minimum ISS value as a function of θ.

In contrast to the isotropic linear-elastic behavior [49], the ISS in the basal plane is evidently anisotropic. Specifically, the polar plot displays a distinct hexagonal structure that is consistent with alternating "hard" and "easy" shear directions that correspond to the maximum and minimum ISS values in the basal plane, respectively. These can be rationalized in terms of the stacking structure of the hcp phase as shown in Fig. 3(a). The open and closed circles represent the two distinct atomic layers in the $\cdots ABABAB \cdots$ stacking of the hcp structure. The six "easy" shear directions are shown by the black arrows and

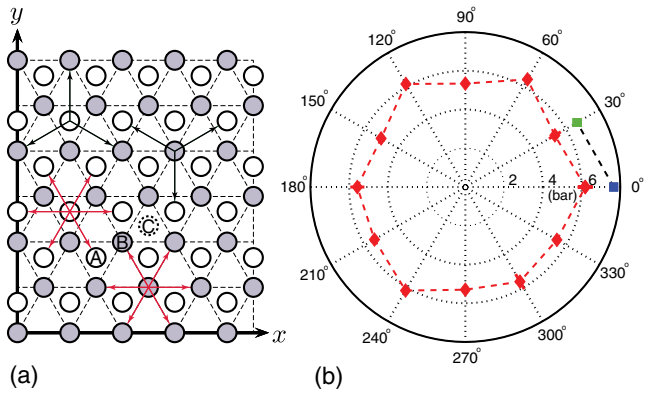

FIG. 3 (color online). Shear directions and anisotropy of the ISS in the basal plane. a) Black (in groups of three) and red (in groups of six) arrows describe the "easy" and "hard" shearing directions, respectively, for the two distinct atomic planes, labeled A and B. Unoccupied position is shown by dashed circle labeled C. b) Polar plot of the minimum ISS as a function of shear direction. Diamonds (red) depict results for the system containing $N = 180$ atoms at $T = 1$ K for $\dot{d} = 1 \times 10^{-6}$ Å per step and $\tau = 1/40$ K^{-1}. Blue (at 0°) and green (at 30°) squares represent results for $N = 480$ at $T = 0.5$ K for $\dot{d} = 2 \times 10^{-6}$ Å per step and $\tau = 1/40$ K for the hard and easy directions, respectively. Error bars are smaller than symbol sizes.

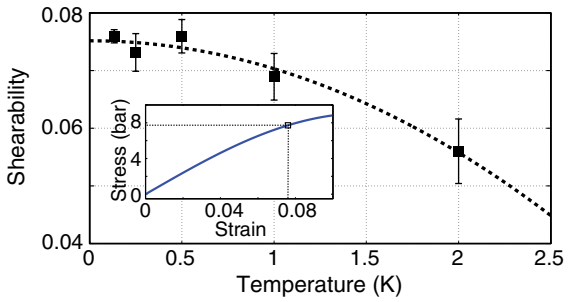

FIG. 4 (color online). Shearability for the easy direction as a function of temperature. Data points represent minimum shearabilities obtained from sets of 15 independent deformation simulations. Error bars represent standard deviations of respective data sets. Dashed line serves as a guide to the eye. Inset displays converged low-temperature limit of the shear stress-strain curve at $T = 0.5$ K. Data point shows estimated shearability and ISS for hcp ^{4}He at a mmolar volume of 21 cm^3.

represent those in which an A or B layer is sheared into the unoccupied C position, producing a SF in the hcp structure. Similarly, the six "hard" directions for both planes are depicted by the red arrows. Within this terminology, the results shown in Figs. 1 and 2 correspond to shear in the hard direction.

The hexagonal shape indicates that the ISS value, for given conditions of deformation, is determined by the shear stress component resolved on the nearest easy direction. This is consistent with Schmid's law of resolved shear stress [50,51], by which the ISS corresponding to a given shear direction in the basal plane is expected to be $\sigma_{\mathrm{ISS}} = \sigma_{\mathrm{min}}/\cos\alpha$, where σ_{min} is the ISS in the easy direction and α is the angle between the applied basal-plane shear and the nearest easy direction. Indeed, the PIMC ratio between the minimum ISS values for the easy and hard directions is estimated to be $\sigma_{\mathrm{min}}/\sigma_{\mathrm{max}} = (1.02 \pm 0.02) \times \frac{1}{2}\sqrt{3}$, in very good agreement with the theoretical ratio of $\frac{1}{2}\sqrt{3}$. This behavior is found to be robust and independent of the simulation conditions. This can be seen, for instance, from the blue and green squares, which represent data for the hard and easy directions, respectively, for $T = 0.5$ K, $\dot{d} = 2 \times 10^{-6}$ Å per MC step and $\tau = 1/40$ K, giving a ratio $\sigma_{\mathrm{min}}/\sigma_{\mathrm{max}} = (1.00 \pm 0.04) \times \frac{1}{2}\sqrt{3}$. These results imply that a single ISS value, e.g., that for the easy direction, is sufficient to fully characterize the entire basal-plane ISS behavior.

While the qualitative character of the ISS profile is independent of the simulation conditions, the quantitative ISS values are not, as can be seen in Fig. 3. In particular, they are found to depend on algorithmic parameters such as system size, deformation rate and time step, as well as the temperature. We have carried out a detailed study of the influence of these parameters, which can be found in the Supplemental Material [48]. The results indicate that, (i) the cell-size convergence of the results is reached for the medium cell (480 atoms), which suggests that the typical nucleation event is characterized by a length scale of the order of ~30 Å, (ii) the deformation-rate dependence is weak, with the results of the two slowest deformation rates varying less than 1% and within 5% of the ideal quasistatic limit, and (iii), the time-step value affects only the critical stress values through the stress-strain curve. In contrast, the shearability results are found to be independent of time step. Based on these results, all remaining simulations were carried out for the easy direction using the medium cell, a time step of $\tau = 1/80$ K^{-1} and a deformation rate of $\dot{d} = 2 \times 10^{-6}$ Å per MC step.

The temperature dependence of the shearability is displayed in Fig. 4. As expected, it reveals a higher shearability for the lower temperatures. For the higher temperatures, the variation with temperature is significant, with the shearability increasing by about 30% between 2 and 1 K. This indicates that in this regime the role of thermal fluctuations is still significant. For 0.5 K and lower temperatures, on the other hand, the shearability reaches a plateau value, suggesting that in this regime the role of thermal fluctuations has become small compared to those of quantum nature and reaching the regime of intrinsic materials response. Estimating it as the average of the results obtained for 0.5, 0.25, and 0.1333 K, we estimate the intrinsic shearability to be $(7.5 \pm 0.3)\%$. Based on the converged 0.5 K elastic stress-strain curve shown in the inset (See Supplemental Material [48]), the corresponding ISS is found to be (7.7 ± 0.3) bar.

Finally, to put these results in a broader perspective, it is useful to analyze them in the general context of ISS for

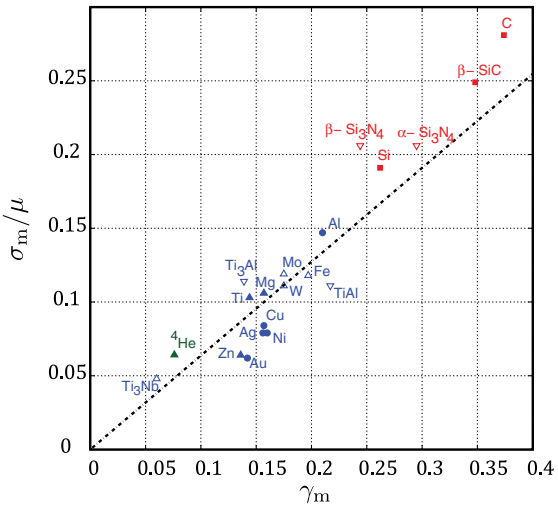

FIG. 5 (color online). Relation between the ISS scaled by the shear modulus and shearability for solids characterized by different crystal structures and bonding types. Line describes Frenkel model (see text). All data points, except for ^{4}He and Ti_3Nb, represent the strain-controlled values reported in Ref. [3]. Different symbols correspond to distinct crystal structures. Blue (all data points left of β-Si_3N_4, except ^{4}He) and red (five rightmost) symbols represent metallic and covalent crystals, respectively. Green filled upward triangle (second data point from the left) represents present PIMC++ result for hcp ^{4}He. Result for Ti_3Nb is based on data from Ref. [52].

crystalline materials. Recently, Ogata *et al.* [3] used density-functional theory calculations to assess the ideal strength of a large number of classical crystalline solids characterized by different crystal structures and bonding types. Measuring the intrinsic shearability at zero temperature, they found it to correlate with the degree of valence-charge localization and directionality of the bonding. Specifically, the results of Ogata *et al.* show that the shearability of a crystal increases with the degree of directionality of the bonding. Accordingly, the shearability of covalent semiconductors is larger than that of metals and within the subgroup of metallic crystals those with some directionality in the bonding are characterized by a larger shearability compared to the noble metals. This is shown in Fig. 5, which displays ISS data scaled by the shear modulus as a function of the shearability for a large number of metals and semiconductor crystals [3].

Moreover, Ogata *et al.* showed that a modified Frenkel model for ideal strength, in which the ISS and shearability are related by $\sigma_m = 2\mu\gamma_m/\pi$, with σ_m the ISS, γ_m the shearability, and μ the shear modulus, gives an approximately universal description of the data as is displayed by the line in Fig. 5.

With our result for the intrinsic ISS in hcp ^{4}He, we can now add a data point to this plot, including a material that is dominated by quantum effects and in which the cohesion is characterized by nondirectional van der Waals forces. The black triangle represents the 0.5 K basal-plane ISS and shearability in the easy direction determined earlier. Surprisingly, the result remains consistent with the picture put forth by Ogata *et al.*: the scaled ISS for hcp ^{4}He falls below that of the group of metals, being governed by entirely nondirectional forces, and is well described by the modified Frenkel model. Interestingly, despite the weakness of the dispersion interactions governing the cohesion in solid Helium, the shearability of hcp solid ^{4}He is still larger than that of the Ti_3Nb gum metal approximant [52].

The fact that our ISS results for the prototypical quantum crystal ^{4}He is well described by purely classical concepts, both in terms of failure mechanism as well as quantitatively, is quite intriguing. Although our data pertain specifically to the case of ISS and homogeneous defect nucleation, they may suggest that the quantum effects that give rise to superfluidity in the liquid phase are significantly less prominent in the crystalline phase. This would also lend support to assumptions in the literature that inherently classical concepts such as the Granato-Lücke model [53–55] remain useful for the description of mechanical behavior of quantum crystals. In addition, it appears consistent with the recent experimental affirmation of the absence of nonclassical rotational inertia effects in torsion-oscillator experiments with solid ^{4}He [28]. Finally, these findings may also be related to the recent controversy [31,32] regarding whether or not the explanation of the observed giant plasticity in crystalline ^{4}He involves nonclassical effects.

E.J.L.B. and M.K. gratefully acknowledge support from the Brazilian agencies CNPq, Fapesp, Capes, and the Center for Computational Engineering and Sciences - Fapesp/Cepid Grant No. 2013/08293-7. E.J.L.B was partially supported by a Santander Graduate Mobility Fellowship. This work was partially supported by the U.S. Department of Energy, Office of Basic Energy Sciences, Division of Materials Sciences and Engineering under Award No. DE-SC0010412 (W.C.). The authors gratefully acknowledge Bryan Clark for his assistance with the PIMC++ code.

*Corresponding author.
dekoning@ifi.unicamp.br
†landinez@ifi.unicamp.br
‡caiwei@stanford.edu

[1] J. Pokluda, M. Černý, P. Šandera, and M. Šob, J. Comput.-Aided Mater. Des. **11**, 1 (2004).
[2] S. Ogata, J. Li, and S. Yip, Science **298**, 807 (2002).
[3] S. Ogata, J. Li, N. Hirosaki, Y. Shibutani, and S. Yip, Phys. Rev. B **70**, 104104 (2004).
[4] S. S. Brenner, J. Appl. Phys. **27**, 1484 (1956).
[5] A. Kelly and N. Macmillan, *Strong Solids*, (Clarendon Press, Oxford, 1986).
[6] O. Rodríguez de la Fuente, J. A. Zimmerman, M. A. González, J. de la Figuera, J. C. Hamilton, W. W. Pai, and J. M. Rojo, Phys. Rev. Lett. **88**, 036101 (2002).

[7] K. J. Van Vliet, J. Li, T. Zhu, S. Yip, and S. Suresh, Phys. Rev. B **67**, 104105 (2003).
[8] C. A. Schuh, J. K. Mason, and A. C. Lund, Nat. Mater. **4**, 617 (2005).
[9] Y. Yue, P. Liu, Z. Zhang, X. Han, and E. Ma, Nano Lett. **11**, 3151 (2011).
[10] J. Alcalá, R. Dalmau, O. Franke, M. Biener, J. Biener, and A. Hodge, Phys. Rev. Lett. **109**, 075502 (2012).
[11] M. Jokl, V. Vitek, and C. McMahon, Jr, Acta Metall. **28**, 1479 (1980).
[12] R. Thomson, in *Solid State Physics*, edited by H. Ehrenreich and D. Turnbull (Academic Press, New York, 1986), Vol. 39, p. 1.
[13] J. R. Rice, J. Mech. Phys. Solids **40**, 239 (1992).
[14] D. Roundy, C. R. Krenn, M. L. Cohen, and J. W. Morris, Jr, Philos. Mag. A **81**, 1725 (2001).
[15] J. Li, K. J. Van Vliet, T. Zhu, S. Yip, and S. Suresh, Nature (London) **418**, 307 (2002).
[16] M. Jahnátek, J. Hafner, and M. Krajčí, Phys. Rev. B **79**, 224103 (2009).
[17] Y. Umeno, Y. Shiihara, and N. Yoshikawa, J. Phys. Condens. Matter **23**, 385401 (2011).
[18] W. Zhou, Y. Zhang, H. Sun, and C. Chen, Phys. Rev. B **86**, 054118 (2012).
[19] P. W. Anderson, *Basic Notions of Condensed Matter Physics* (Benjamin-Cummings, Menlo Park, CA, 1984).
[20] E. Kim and M. Chan, Nature (London) **427**, 225 (2004).
[21] E. Kim and M. H. W. Chan, Science **305**, 1941 (2004).
[22] J. T. West, O. Syshchenko, J. Beamish, and M. H. W. Chan, Nat. Phys. **5**, 598 (2009).
[23] J. Day, O. Syshchenko, and J. Beamish, Phys. Rev. B **79**, 214524 (2009).
[24] X. Rojas, A. Haziot, V. Bapst, S. Balibar, and H. J. Maris, Phys. Rev. Lett. **105**, 145302 (2010).
[25] S. Balibar, A. Fefferman, A. Haziot, and X. Rojas, J. Low Temp. Phys. **168**, 221 (2012).
[26] J. Beamish, J. Low Temp. Phys. **168**, 194 (2012).
[27] D. Y. Kim, J. T. West, T. A. Engstrom, N. Mulders, and M. H. W. Chan, Phys. Rev. B **85**, 024533 (2012).
[28] D. Y. Kim and M. H. W. Chan, Phys. Rev. Lett. **109**, 155301 (2012).
[29] A. Haziot, X. Rojas, A. D. Fefferman, J. R. Beamish, and S. Balibar, Phys. Rev. Lett. **110**, 035301 (2013).
[30] M. Chan, R. Hallock, and L. Reatto, J. Low Temp. Phys. **172**, 317 (2013).
[31] C. Zhou, C. Reichhardt, M. J. Graf, J.-J. Su, A. V. Balatsky, and I. J. Beyerlein, Phys. Rev. Lett. **111**, 119601 (2013).
[32] A. Haziot, X. Rojas, A. D. Fefferman, J. R. Beamish, and S. Balibar, Phys. Rev. Lett. **111**, 119602 (2013).
[33] M. A. Paalanen, D. J. Bishop, and H. W. Dail, Phys. Rev. Lett. **46**, 664 (1981).
[34] D. M. Ceperley, Rev. Mod. Phys. **67**, 279 (1995).
[35] D. M. Ceperley and B. Bernu, Phys. Rev. Lett. **93**, 155303 (2004).
[36] B. K. Clark and D. M. Ceperley, Comput. Phys. Commun. **179**, 82 (2008).
[37] M. Boninsegni, N. Prokof'ev, and B. Svistunov, Phys. Rev. Lett. **96**, 105301 (2006).
[38] M. Boninsegni, A. B. Kuklov, L. Pollet, N. V. Prokof'ev, B. V. Svistunov, and M. Troyer, Phys. Rev. Lett. **97**, 080401 (2006).
[39] L. Pollet, M. Boninsegni, A. B. Kuklov, N. V. Prokof'ev, B. V. Svistunov, and M. Troyer, Phys. Rev. Lett. **98**, 135301 (2007).
[40] L. Pollet, M. Boninsegni, A. B. Kuklov, N. V. Prokof'ev, B. V. Svistunov, and M. Troyer, Phys. Rev. Lett. **101**, 097202 (2008).
[41] S. G. Söyler, A. B. Kuklov, L. Pollet, N. V. Prokof'ev, and B. V. Svistunov, Phys. Rev. Lett. **103**, 175301 (2009).
[42] L. A. P. Ardila, S. A. Vitiello, and M. de Koning, Phys. Rev. B **84**, 094119 (2011).
[43] J. Frenkel, Z. Phys. **37**, 572 (1926).
[44] W. Krauth, *Statistical Mechanics: Algorithms and Computations* (Oxford University Press Oxford, 2006).
[45] R. A. Aziz, A. R. Janzen, and M. R. Moldover, Phys. Rev. Lett. **74**, 1586 (1995).
[46] D. M. Ceperley and E. L. Pollock, Phys. Rev. Lett. **56**, 351 (1986).
[47] B. Bernu and D. Ceperley, in *Quantum Simulations of Complex Many-Body Systems: From Theory to Algorithms*, NIC Series, edited by A. M. J. Grotendorst, and D. Marx (John von Neumann Institute for Computing, Jülich, 2002), Vol. 10 p. 51.
[48] See Supplemental Material at http://link.aps.org/supplemental/10.1103/PhysRevLett.112.155303 for further technical details of the PIMC calculations.
[49] J. F. Nye, *Physical Properties of Crystals* (Oxford University Press, Oxford, 1985).
[50] E. Schmid and W. Boas, *Plasticity of Crystals: with Special Reference to Metals* (Chapman & Hall, London, 1968).
[51] F. R. N. Nabarro, Philos. Mag. **14**, 861 (1966).
[52] N. Nagasako, R. Asahi, and J. Hafner, Phys. Rev. B **85**, 024122 (2012).
[53] A. Granato and K. Lucke, J. Appl. Phys. **27**, 583 (1956).
[54] P. Corboz, L. Pollet, N. V. Prokof'ev, and M. Troyer, Phys. Rev. Lett. **101**, 155302 (2008).
[55] A. D. Fefferman, F. Souris, A. Haziot, J. R. Beamish, and S. Balibar, Phys. Rev. B **89**, 014105 (2014).